# Multifunctional Integrated Photonic Switches

Hilmi Volkan Demir, Vijit A. Sabnis, Onur Fidaner, *Student Member, IEEE*, Jun-Fei Zheng, James S. Harris, Jr., *Fellow, IEEE*, and David A. B. Miller, *Fellow, IEEE*

***Abstract*—Traditional optical-electronic-optical (o-e-o) conversion in today's optical networks requires cascading separately packaged electronic and optoelectronic chips and propagating high-speed electrical signals through and between these discrete modules. This increases the packaging and component costs, size, power consumption, and heat dissipation. As a remedy, we introduce a novel, chip-scale photonic switching architecture that operates by confining high-speed electrical signals in a compact optoelectronic chip and provides multiple network functions on such a single chip. This new technology features low optical and electrical power consumption, small installation space, high-speed operation, two-dimensional scalability, and remote electrical configurability.**

**In this paper, we present both theoretical and experimental discussion of our monolithically integrated photonic switches that incorporate quantum-well waveguide modulators directly driven by on-chip surface-illuminated photodetectors. These switches can be conveniently arrayed two-dimensionally on a single chip to realize a number of network functions. Of those, we have experimentally demonstrated arbitrary wavelength conversion across 45 nm and dual-wavelength broadcasting over 20 nm, both spanning the telecommunication center band (1530–1565 nm) at switching speeds up to 2.5 Gb/s. Our theoretical calculations predict the capability of achieving optical switching at rates in excess of 10 Gb/s using milliwatt-level optical and electrical switching powers.**

***Index Terms*—Integrated optoelectronic devices, modulators, photonic switches, quantum-well (QW) devices.**

## I. Introduction

THE rapid growth in Internet traffic around the globe, for example, in Northern America, Japan, and Europe [1]–[4], will necessitate improvements in today's optical communication technology; the present optical networks are, however, limited in a number of ways by electronics conventionally utilized in optical-electronic-optical (o-e-o) conversion. For that, there is a need for investigating and developing new integrated photonic platforms to accommodate the traffic growth. In this paper, we present a chip-scale photonic switching technology [5], [6], as shown in Fig. 1, which simultaneously offers multiple network functions for multiple channels on a single chip and potentially provides a scalable photonic switching platform [7] for next generation cost-efficient optical networks.

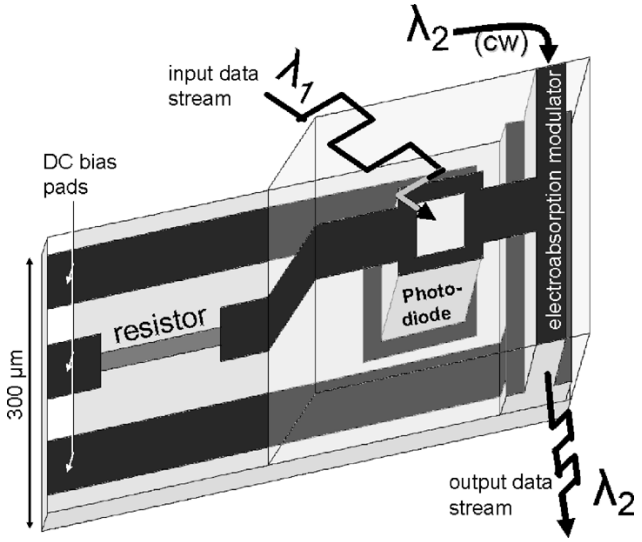


Fig. 1. Illustration of an integrated photonic switch.

Complex data processing, routing, and switching in optical network nodes currently requires employing o-e-o conversion. This technology comprises serially cascading multiple, separately-packaged optoelectronic and electronic components. Although o-e-o conversion is a mature technology, it suffers from several disadvantages [8]. Since high-speed electrical signal propagation between discrete components is required, packaging costs are substantial and grow as the number of discrete components increases. Moreover, existing technology requires large installation space, introducing additional complexities in system design. High-power consumption and heat dissipation are also significant problems in traditional o-e-o systems.

Integrated photonic switches [9]–[15] avoid the aforementioned disadvantages and can supplant traditional o-e-o conversion for certain network applications. Our research group has proposed different schemes of integrated photonic switches [16], [17] and has briefly presented different generations of such photonic switches [5]–[7], [9], [16]–[20]. Here, we will discuss the device in greater depth. First, in Section II, we will present the switching structure to discuss its operation principles. In Section III, we will derive an equation to design switches with a desired bandwidth and contrast ratio and present results from a simulation showing the feasibility of 10 Gb/s operation. Following that, in Section IV, we will discuss some of the details of the fabrication, including the epitaxial layer design and its relevance to the electroabsorption properties and the integration of

Manuscript received July 16, 2004; revised November 5, 2004. This work was supported by Intel Corporation and by Photonics Technology Access Program (funded by The National Science Foundation and the Defense Advanced Research Projects Agency).

H. V. Demir is with Edward L. Ginzton Laboratory and Solid State and Photonics Laboratory, Stanford University, Stanford, CA 94305 USA. He is also with Nanotechnology Research Center, Bilkent University, Ankara 06800 Turkey (e-mail: volkan@bilkent.edu.tr).

V. A. Sabnis is with Edward L. Ginzton Laboratory and Solid State and Photonics Laboratory, Stanford University, Stanford, CA 94305, USA. He is also with Translucent, Inc., Palo Alto, CA 94303 USA.

O. Fidaner, J. S. Harris, and D. A. B. Miller are with Edward L. Ginzton Laboratory and Solid State and Photonics Laboratory, Stanford University, Stanford, CA 94305 USA.

J. F. Zheng is with Intel Strategic Technology, Intel Corporation, Santa Clara, CA 95052 USA.

Digital Object Identifier 10.1109/JSTQE.2004.841715

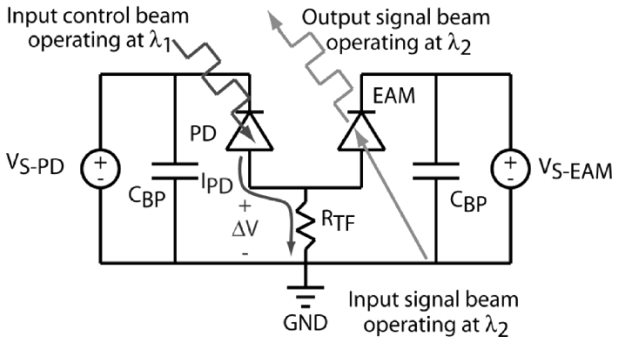


Fig. 2. Simplified circuit diagram of the integrated photonic switch and illustration of its operation.

the two major elements in our structure. Finally, in Section V, we will present experimental results highlighting the characteristics of the switch operation and demonstrating the multiple network functions provided by these switches.

## II. Switch Structure and Operation

Fig. 2 shows a simplified circuit diagram, neglecting parasitics, of our integrated photonic switch. The switch comprises two subcircuits: the left-side circuit consists of a $p-i-n$ diode photodetector (PD) connected to a bias supply $V_{S-PD}$ with a local parallel bypass capacitor $C_{BP}$, while the right-side circuit similarly consists of a $p-i-n$ diode, multiple-quantum-well (MQW) waveguide electroabsorption modulator (EAM) connected to a separate bias supply $V_{S-EAM}$ with another local parallel bypass capacitor. The $p$-contacts of both diodes are connected together using a high-speed, low-parasitic electrical interconnect and attach to one end of an integrated thin film resistor $R_{TF}$, which subsequently terminates at the ground pad, GND. The switch requires two optical inputs, consisting of a continuous-wave signal beam incident on one end of the modulator waveguide and a control beam data stream incident on the photodetector, and two electrical inputs, consisting of the PD and EAM bias voltages. The output of the switch consists of the signal beam exiting the opposite end of the EAM waveguide encoded with the control beam data. The switch operates, as shown in Fig. 2, in the following manner.

1) To enable the switch, we apply appropriate biases to the PD and EAM. The PD bias is chosen such that linear photocurrent extraction is always maintained. This requires a PD intrinsic-region electric field $> 50$ kV/cm [21] to ensure saturated electron and hole carrier velocities. Note that by slightly forward biasing the PD, photocurrent extraction can be eliminated, disabling the functionality of the switch. The EAM bias is chosen such that its MQWs strongly absorb at the output signal beam wavelength. The value of the EAM bias will depend on the signal beam wavelength and the electroabsorption characteristics at this wavelength. (In some applications, we would want the EAM to be transparent when the switch is disabled, in which case we would also choose a specific EAM bias (e.g., zero bias or forward bias) for transparency in the disabled state.)

2) We couple a continuous-wave signal beam into the input side of the EAM waveguide. Due to the EAM supply voltage, the QWs, located in the core of the EAM waveguide, heavily absorb the signal beam, resulting in approximately zero optical transmission at the output end of the waveguide.

3) We illuminate the PD with a control beam data stream.

4) The PD converts the incident optical data stream to an electrical photocurrent data stream.

5) The PD photocurrent charges the capacitances of the PD and EAM, which are subsequently discharged through the on-chip resistor. This process creates a voltage drop across the resistor corresponding to the data carried by the photocurrent. This voltage drop, in turn, effectively reduces the voltage across the EAM.

6) Through the quantum-confined Stark effect (QCSE) [22], this reduction in EAM voltage decreases the MQW absorption at the signal beam wavelength. If the EAM voltage swing significantly reduces the QW absorption, then the signal beam transmission substantially increases. Hence, the circuit functions as a noninverting optical switch, transferring data from the input control beam incident on the PD to the signal beam propagating through the EAM waveguide.

An alternative approach to understanding the switching behavior of PD-EAM integrated photonic switch (IPS) is to consider a simple load line analysis of the circuit as exemplified in Fig. 3. The EAM current is given by

$$I_{EAM} = \frac{\eta q P_{\text{sig}}}{\hbar\omega}\left(1 - e^{-\Gamma_{MQW}\alpha(\lambda_{\text{sig}}, V_{EAM})L}\right), \qquad (1)$$

where $\eta$ is the quantum efficiency, $P_{\text{sig}}$ is the coupled signal power in the waveguide, $\Gamma_{MQW}$ is the spatial overlap integral of the signal beam optical mode with the QWs, $\alpha(\lambda_{\text{sig}}, V_{EAM})$ is the absorption coefficient at the signal wavelength for a particular $V_{EAM}$, and $L$ is the waveguide length. From a load line analysis, the EAM current also equals

$$I_{EAM} = \frac{V_{S-EAM} - V_{EAM}}{R} - I_{PD}. \qquad (2)$$

As an example, in Fig. 3(a), we plot $I_{EAM}$ versus $V_{EAM}$ along with the corresponding load line equation given earlier. For signal beam wavelengths below the heavy hole-electron exciton absorption peak, through the QCSE, the absorption from the QWs increases with increasing voltage [Fig. 3(b)] resulting in a larger photocurrent flowing through the EAM. The optical transmission through the device correspondingly decreases with increasing voltage as shown in Fig. 3(c). When the control beam is incident on the photodetector, creating a photocurrent, the load line shown in Fig. 3(a) moves downward, reducing the EAM current and voltage operating points. This reduction in EAM voltage decreases the QW absorption [Fig. 3(b)] and, hence, increases the optical transmission through the EAM [Fig. 3(c)].

The inclusion of bypass capacitors on chip, or as a part of an appropriately designed electrical probe, ensures localized optoelectronic switching without loading from external circuit components. The bypass capacitors function as low-pass filters and confine all high-speed electrical signals to the area of the PD and EAM only. This allows high-speed switching using low optical powers since only the small capacitances of the PD and EAM need to be charged and discharged. For this device architecture,

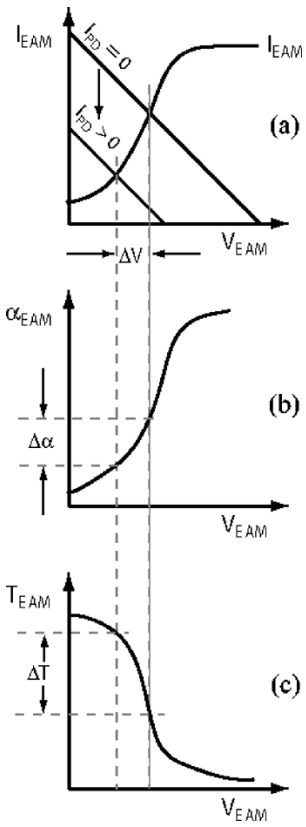


Fig. 3. Load-line analysis of integrated photonic switch circuit: The photodiode current reduces the voltage across the EAM in (a), correspondingly decreases the MQW absorption of the EAM in (b), and increases the transmission through the EAM in (c).

the 3-dB electrical bandwidth of $|V_{EAM}(\omega)/I_{PD}(\omega)|$, ignoring the effects of the EAM current source and any parasitics, is approximately given by

$$f_{3dBe} = \frac{\sqrt{3}}{2\pi R_{TF}(C_{PD} + C_{EAM})}. \tag{3}$$

To achieve a desired switching bandwidth, the effective RC time constant needs to be engineered. In this case, $C_{PD}$ and $C_{EAM}$, the PD and EAM internal device capacitances, respectively, can be modified through appropriate choice of the epitaxial layer design and the geometry of the individual devices in conjunction with the thin film resistor $R_{TF}$.

## III. Switch Design

### A. Design Guidelines

A first-order analysis of the integrated switch circuit provides a set of general design guidelines. The change in the electric field across the EAM $\Delta E_{EAM}$ can be calculated assuming that the photogenerated charge at the PD is distributed between the EAM and the PD capacitors $C_{EAM}$ and $C_{PD}$, respectively

$$\Delta E_{EAM} = \frac{\Delta V_{EAM}}{t_{EAM}} = \frac{Q_{\text{inj}}}{t_{EAM}(C_{PD} + C_{EAM})} = \frac{Q_{\text{inj}}}{\varepsilon\left(A_{PD}\frac{t_{EAM}}{t_{PD}} + A_{EAM}\right)}. \tag{4}$$

In this simple formulation, the effects of the bypass capacitors, loading from external circuitry, and the voltage discharge through the on-chip resistor have been excluded. Also, the effective dielectric constant is assumed to be the same for both the PD and the EAM intrinsic regions. In (4), $\Delta V_{EAM}$ is the optically-induced voltage swing across the EAM; $Q_{\text{inj}}$ is the injected charge from the control beam; $A_{PD}$ and $A_{EAM}$ are the horizontal cross section areas of the PD and the EAM, respectively; and $t_{PD}$ and $t_{EAM}$ are the intrinsic region thicknesses of the PD and EAM, respectively.

We can use (1)–(4) to design a switch with a minimum optical control beam input power for switch operation at a particular data rate and contrast ratio for the signal beam exiting the EAM. Equation (4) indicates that to minimize the injected charge and, hence, the optical power on the PD, for a required $\Delta E_{EAM}$, we need to minimize the junction areas of the PD and the EAM, increase $t_{PD}$, and decrease $t_{EAM}$. $A_{EAM}$ and $A_{PD}$ are limited by fabrication requirements, the latter also limiting the power handling capability of the PD. On the other hand, $t_{PD}$ cannot be increased arbitrarily to avoid carrier transit time limitations and reduced optical power handling capability. Furthermore, $t_{EAM}$ should be greater than 0.25 $\mu$m to achieve a reasonable overlap between the optical mode and the electroabsorption layers and to avoid excessive optical loss due to free carrier absorption arising from mode field penetration into the doped waveguide layers. From (3), we see that it is necessary to minimize the RC time constant for faster operation. For a given time constant, large on-chip $R$ is preferred to optically-induce a larger voltage swing, to ease fabrication tolerances, and to reduce sensitivity of the switch performance on the device contact resistance. For that, both $C_{PD}$ and $C_{EAM}$ should be minimized, which will also minimize the required optical power. However, the EAM capacitance should dominate the PD capacitance to minimize the required input charge for a desired $\Delta E_{EAM}$, due to the $t_{EAM}$ factor in the denominator of (4).

We can also relate these parameters to contrast ratio. Assuming the absorption coefficient changes by $\Delta\alpha$ when the electric field changes by $\Delta E_{EAM}$ we get

$$\begin{aligned} CR_{dB} &= 10\log_{10}(\Delta T) \\ &= 10\log_{10}\left(e^{-\Gamma_{MQW}\Delta\alpha(\lambda_{\text{sig}},V_{EAM},\Delta E_{EAM})L_{EAM}}\right) \\ &= 4.343\Delta\alpha\Gamma_{MQW}L_{EAM}. \end{aligned} \tag{5}$$

Using this in (4), noting that $A_{\text{EAM}} = \text{w}_{\text{EAM}}\text{L}_{\text{EAM}}$, we get

$$Q_{\text{inj}} = \frac{\varepsilon\left(\Delta\alpha A_{PD}\frac{t_{EAM}}{t_{PD}} + \frac{w_{EAM}CR_{dB}}{4.343\Gamma_{MQW}}\right)}{\frac{\Delta\alpha}{\Delta E_{EAM}}} \tag{6}$$

where $\Delta\alpha/\Delta E_{EAM}$ is a fundamental characteristic of the electroabsorption layers used in the EAM. This characteristic is strongly wavelength and electric field dependent and is determined by the electroabsorption layer design and growth quality. To minimize the required injected charge from the control beam, the electroabsorption material should be grown and designed with as large a $\Delta\alpha/\Delta E_{EAM}$ as possible in the wavelength range of interest.

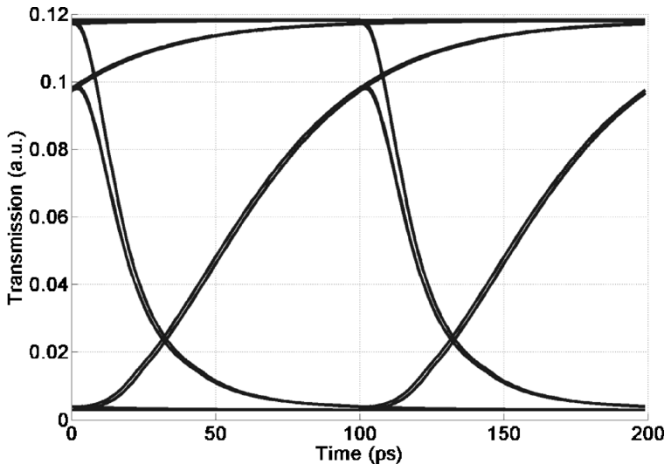


Fig. 4. Simulated modulator transmission with >10 dB extinction ratio at 10 Gb/s.

### *B. Simulations*

Using a circuit model that includes both the integrated photonic switch as well as the off-chip bias circuitry (voltage supplies and an electrical probe incorporating bypass capacitors), we can simulate device performance, and can make some predictions of the device performance that might be obtained under the best conditions. Specifically, the simulation of Fig. 4 shows the feasibility of optical switching at 10 Gb/s for a 10-dB extinction ratio using 7 mW of average absorbed optical power. Fig. 4 shows the open eye diagram of the simulated switch structure at 10 Gb/s.

In this simulation, we use empirical data from Zhang [23] for the electroabsorption spectra. We consider a PD with a 30 $\times$ 30 $\mu$m mesa and an intrinsic region of 1.25 $\mu$m, resulting in a diode capacitance of 76 fF, parasitic capacitance of 15 fF, and internal resistance of 39$\Omega$. The EAM is simulated to have an area of 2 $\times$ 300 $\mu$m with 0.37-$\mu$m intrinsic region thickness, giving diode capacitance of 153 fF, parasitic capacitance of 24 fF, and internal resistance of 120$\Omega$. This simulation implies that contact resistances and the parasitics have to be minimized for a successful 10-Gb/s demonstration. This simulation, however, indicates the high device performance may be feasible with this approach.

## IV. Implementation of the Switch

In this section, we will outline the epitaxial layer design of the EAM and PD, summarize the mask design, and conclude with the expected device switching bandwidths.

### *A. EAM Epitaxial Layer Design*

For the electroabsorption, we employed the QCSE, rather than the Franz–Keldysh effect, which is observed in bulk semiconductors. Although bulk semiconductor layers may provide a wider wavelength band of operation, QWs provide a stronger change in absorption per unit change in perpendicular electric field $(\Delta\alpha/\Delta E_{\mathrm{EAM}})$ [11]. Moreover, QW modulators typically require about half as much voltage swing compared to bulk modulators, reducing the optical input power requirements of our switch. Our QWs include ten 80-Å-thick, 0.8% compressively strained, 1.56-Q InGaAsP wells with 60-Å-thick, $-0.5\%$ tensile strained, 1.22-Q InGaAsP barriers. This MQW structure exhibits a photoluminescence peak wavelength between 1480 and 1490 nm and is optimally detuned from the C-band (1530–1565 nm) for large optical transmission modulation over this wavelength range.

TABLE I
Epitaxial Layer Design of the EAM

| | Material and Thickness | | Doping ($cm^{-3}$) |
|---|---|---|---|
| 19 | 500 Å InGaAs | | p-Zn, $1.00x10^{19}$ |
| 18 | 10000 Å InP | | p-Zn, $5.00x10^{17}$ |
| 17 | 3000 Å InP | | p-Zn, $1\text{-}5x10^{17}$ |
| 16 | 1950 Å InP | | u.i.d |
| 15 | 200 Å 1.1Q $In_xGa_{1-x}As_yP_{1-y}$ | | u.i.d |
| 14 | 200 Å 1.2Q $In_xGa_{1-x}As_yP_{1-y}$ | | u.i.d |
| 13 | 200 Å 1.3Q $In_xGa_{1-x}As_yP_{1-y}$ | | u.i.d |
| 12 | 60 Å 1.22Q $In_xGa_{1-x}As_yP_{1-y}$ | (x 10) | u.i.d |
| 11 | 80 Å 1.56Q $In_xGa_{1-x}As_yP_{1-y}$ | | u.i.d |
| 10 | 60 Å 1.22Q $In_xGa_{1-x}As_yP_{1-y}$ | | u.i.d |
| 9 | 200 Å 1.3Q $In_xGa_{1-x}As_yP_{1-y}$ | | u.i.d |
| 8 | 200 Å 1.2Q $In_xGa_{1-x}As_yP_{1-y}$ | | u.i.d |
| 7 | 200 Å 1.1Q $In_xGa_{1-x}As_yP_{1-y}$ | | u.i.d |
| 6 | 390 Å InP | | u.i.d |
| 5 | 8500 Å InP | | n-Si, $5.0x10^{17}$ |
| 4 | 200 Å 1.3Q $In_xGa_{1-x}As_yP_{1-y}$ | | n-Si, $3.0x10^{18}$ |
| 3 | 5500 Å InP | | n-Si, $5.0x10^{17}$ |
| 2 | 200 Å 1.3Q $In_xGa_{1-x}As_yP_{1-y}$ | | u.i.d |
| 1 | 2500 Å InP | | u.i.d |
| 0 | (substrate) SI InP | | Fe |

u.i.d: unintentionally doped
SI: semi insulating

Table I lists the epitaxial layer structure, comprising a $p-i-n$ diode, for the EAM. Using a semi-insulating (Fe-doped) substrate substantially reduces the EAM and PD device capacitances and electrically isolates the PD from the EAM, enabling independent operation of both devices. Etch stop layers 2 and 4 are employed to achieve a flat surface after the PD mesa etch and the EAM n-island etch, respectively. InP layer 3, between these two etch-stops, is the seed material for selective area regrowth of the PD epitaxy and is thick enough to prevent punch-through of the PD mesa etch past the lower etch-stop layer. The InP layer 5 serves primarily as the bottom waveguide cladding. We made this layer quite thick to ensure that the dry etch defining the ridge waveguides stops within this layer over the entire two inch EAM wafer. Next, the structure comprises a 0.5 $\mu$m-thick intrinsic region (layers 6–16) that contains a set of MQW electroabsorption layers. Layers 11 and 12 are repeated together and, in conjunction with layer 10, form ten MQWs. Surrounding the MQW layers are a pair of graded heterojunction layers that serve as graded index structures for achieving a symmetrical optical mode around the MQW and for reducing carrier pileup at heterojunction interfaces. The latter is particularly important for holes, since hole pileup at a nongraded InGaAsP-InP interface is likely to degrade the optical transmission modulation and the switching bandwidth. Layer 16 serves as a $p$-dopant offset layer to minimize $p$-dopant diffusion into the MQW region for better electroabsorption and to avoid an increase in EAM junction capacitance. The doping in layer 17 is graded for the same purpose.

TABLE II
EPITAXIAL LAYER DESIGN OF THE PD

| | Material and Thickness | | Doping ($cm^{-3}$) |
|---|---|---|---|
| 13 | 500 Å InGaAs | | p-Zn, $1.00x10^{19}$ |
| 12 | 1000 Å InP | | p-Zn, $3.00x10^{18}$ |
| 11 | 2300 Å InP | | p-Zn, $5.00x10^{17}$ |
| 10 | 3000 Å InP | | p-Zn, $1\text{-}5x10^{17}$ |
| 9 | 1500 Å InP | | u.i.d |
| 8 | 200 Å 1.1Q $In_xGa_{1-x}As_yP_{1-y}$ | | u.i.d |
| 7 | 200 Å 1.2Q $In_xGa_{1-x}As_yP_{1-y}$ | | u.i.d |
| 6 | 200 Å 1.3Q $In_xGa_{1-x}As_yP_{1-y}$ | | u.i.d |
| 5 | 12500 Å InGaAs | | u.i.d |
| 4 | 3300 Å InP | | n-Si, $3.0x10^{17}$ |
| 3 | 5500 Å InP (Si, $5.0x10^{17}$) | | n-Si, $5.0x10^{17}$ |
| 2 | 200 Å 1.3Q $In_xGa_{1-x}As_yP_{1-y}$ | EAM layers | u.i.d |
| 1 | 2500 Å InP | | u.i.d |
| 0 | (substrate) SI InP | | Fe |

u.i.d: unintentionally doped
SI: semi insulating

The EAM epitaxial layers are designed to provide single-transverse-mode waveguide operation over the C-band for 2–5 $\mu$m wide ridge waveguides that are etched into layer 5 or deeper and surrounded by a low index planarization/passivation material (e.g., bisbenzocyclobutene). $\Gamma_{MQW}$ is approximately constant between 0.28–0.30 over this wavelength range. In this waveguide design the overlap integrals of the optical mode with the $p$-doped and $p+$ doped epitaxial layers are negligibly small, ensuring free carrier absorption does not cause excessive propagation loss.

### B. PD Epitaxial Layer Design

The PD was grown via selective area regrowth (SAR) on top of the EAM layer 3. [24] Table II lists the epitaxial layer structure used for the PD. The structure is a simple $p-i-n$ diode comprising a 1.25 $\mu$m thick InGaAs absorber region (layer 5) that strongly absorbs over the 1.3–1.6-$\mu$m telecommunication wavelength band. This enables the IPS to perform unconstrained, bidirectional wavelength conversion over the entire C-band (1530–1565 nm). The theoretical responsivity of the PD is $\sim$0.7 A/W around 1.55 $\mu$m.

Provided the carriers travel at their saturated velocities throughout the 1.46-$\mu$m-thick intrinsic region, this PD structure offers a carrier transit time bandwidth exceeding 30 GHz. This ensures that the switching bandwidth will be determined by the RC time constant of the circuit, rather than a convolution of both effects. Relatively thin intrinsic regions, such as the one we used here, are more suitable for high-power PD operation since the carriers need to travel a smaller distance to reach the contacts, precluding the buildup of large space-charge fields that can substantially alter the electric field and carrier velocities within the intrinsic region. Furthermore, the graded heterostructure layers 6 to 8 significantly reduce hole pile-up between the intrinsic region and the $p$-contact.

### C. Realization of the Switch

Although the discussion in Section III shows the feasibility of faster operation of the IPS, in this proof-of-concept demonstration, we made conservative design choices to ensure the successful fabrication and operation of these devices. The EAM waveguides were 2–5 $\mu$m wide by 300 $\mu$m long, possessing capacitances ranging from 140–370 fF. The PD mesas were 30 $\times$ 30 $\mu$m, possessing a capacitance of 75 fF. TaN thin-film resistors of 340 and 650 $\Omega$ were used on the InP substrate. From (3), these devices nominally have 3-dB electrical switching bandwidths in the range of 1–3.5 GHz. However, the practically realized switching bandwidths are degraded by the presence of parasitic series resistances associated with the PD and EAM arising from suboptimal fabrication procedures.

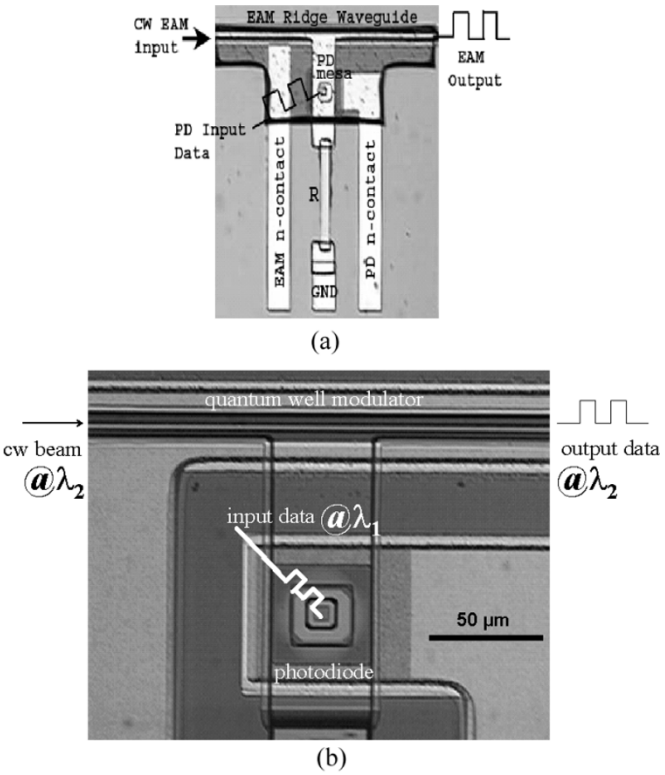


Fig. 5. (a) Plan view of the integrated device and (b) PD and EAM integration right before final metallization.

Fig. 5 shows a fabricated switch employing monolithic integration of the PD and the EAM to realize the circuit proposed in Fig. 2. For simplicity, the bypass capacitors are not included as a part of the fabrication process, but instead are conveniently provided by an external electrical probe. The switch operation requires intimate integration and high-speed interconnection of the EAM and the PD. As a consequence of our SAR technique, the minimum PD–EAM separation is 50 $\mu$m [24]. The overall thickness of the PD structure is chosen such that the uppermost layers of the EAM and the PD are approximately level, enabling metallization to interconnect the $p$-contacts of the two devices. Nonplanarity across the wafer, however, can be accommodated using our new self-aligned planarization and passivation technique [25], [26]. The benzocyclobutene (BCB) polymer fills in the space between the PD mesa and the waveguide EAM such that the polymer surrounding each device is level with its device top within atomic scale flatness. The metal line that interconnects the $p$-contacts overlays this polymer and proceeds

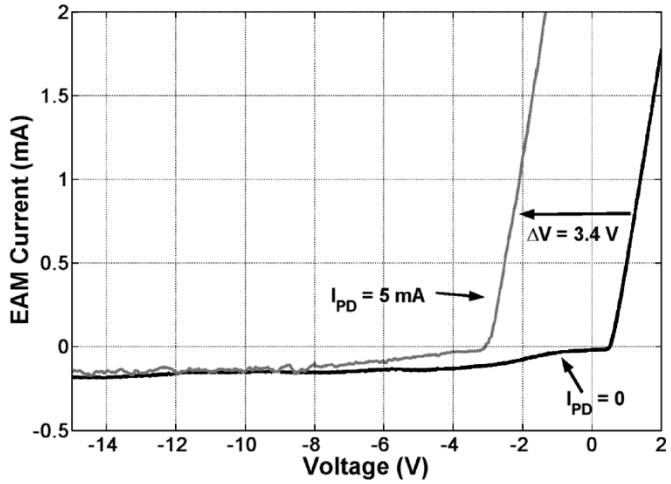


Fig. 6. EAM current versus supply voltage with $I_{PD} = 0$ and $I_{PD} = 5$ mA, demonstrating optical control of EAM voltage.

smoothly down to the substrate level to make contact with the on-chip thin film resistor.

## V. Switch Characterization and Testing

As a first demonstration of successful integration, we present the influence of the control beam on the IV curve of the EAM. In Fig. 6, we observe the IV curve of the EAM in the presence of the control beam to be shifted to the left (larger reverse biases) by 3.4 V. This voltage swing corresponds to the voltage drop across the TaN pull-up resistor due to the photodiode current (i.e., $I_{PD} \times R_{TaN}$). Note that the change in EAM voltage also causes a change in EAM current. The exact voltage shift can be determined using the load line analysis discussed in Section II. In this particular experiment, the EAM current level is small (few hundred microampers), and thus has a negligible effect on the voltage shift. The 3.4-V swing induces an electric field reduction of 6.8 V/$\mu$m across the QWs of the EAM. This is a substantial field swing that can be used to create large changes in transmission through the EAM, as characterized for TE and TM polarized light in Fig. 7. Note that the input data stream, whose polarization is unknown, is incident on the PD mesa, whose operation is independent of the input polarization, and that the EAM polarization dependence, therefore, does not affect the switch operation. Incidentally, this field swing exceeds the modulation requirements of many state-of-the-art RF-driven MQW EAMs. For example, using a waveguide configuration and an active region design similar to ours, Zhang [23] has demonstrated electrically-driven MQW waveguide EAMs exhibiting 10 dB and >20 dB extinction ratios using field swings of only 2.18 and 3.26 V/$\mu$m, respectively.

We also investigated the dependence of the optically-induced voltage swing on the EAM input power. In general, for a given electroabsorption spectrum, as the EAM input power increases, the PD input current required to maintain a certain voltage swing also increases. As seen in the example load-line analysis of Fig. 8, this is a fundamental property of the IPS architecture and needs to be carefully considered when designing an IPS for a particular fiber-coupled output power.

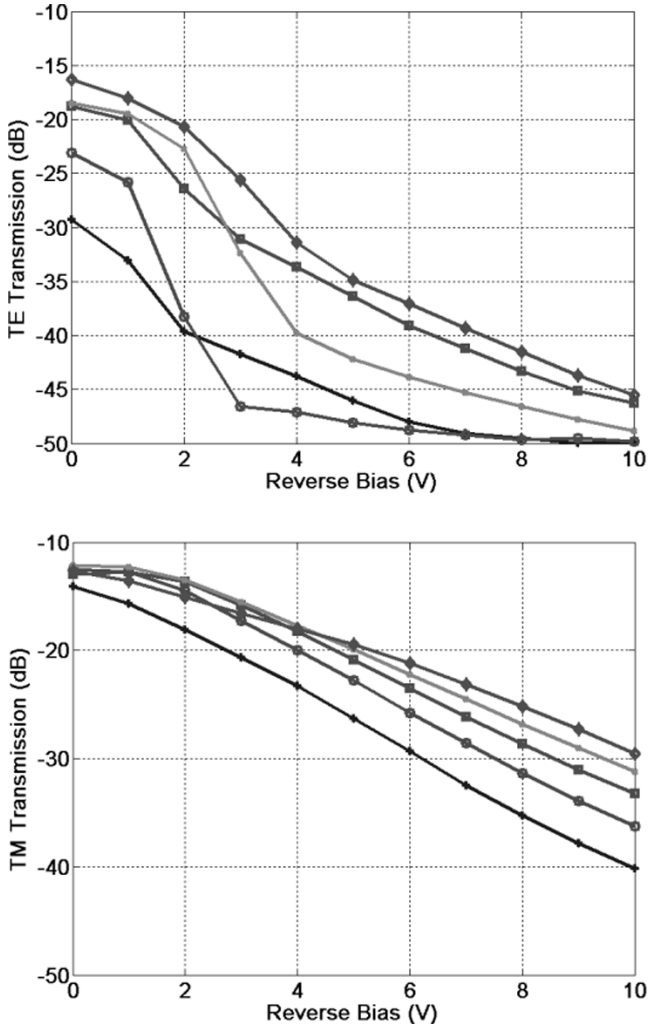


Fig. 7. EAM fiber-to-fiber transmission for TE (top) and TM (bottom) polarized light. Legend: + 1530 nm; ∘ 1538.75 nm; □ 1547.5 nm; × 1556.25 nm; △ 1565 nm.

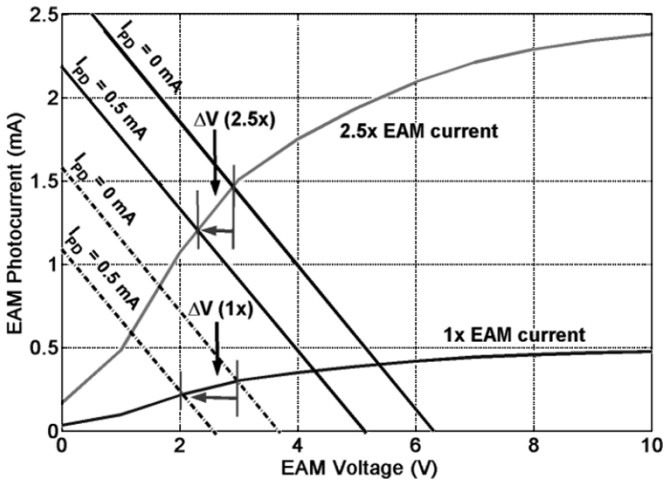


Fig. 8. Load line analysis illustrating optically-induced voltage swing dependence on the EAM current level. The upper curve is simply the lower curve multiplied by 2.5, simulating an increase in the input power of the EAM. In the 1x case the optically-induced voltage swing is 1 V, whereas it is 0.7 V in the 2.5x case; both for a PD current of 0.5 mA. This difference of 0.3 V in the induced voltage swing can change the transmission substantially.

In the experimental setup, single mode tapered fibers couple light to and from the input and the output ends of the waveguide.

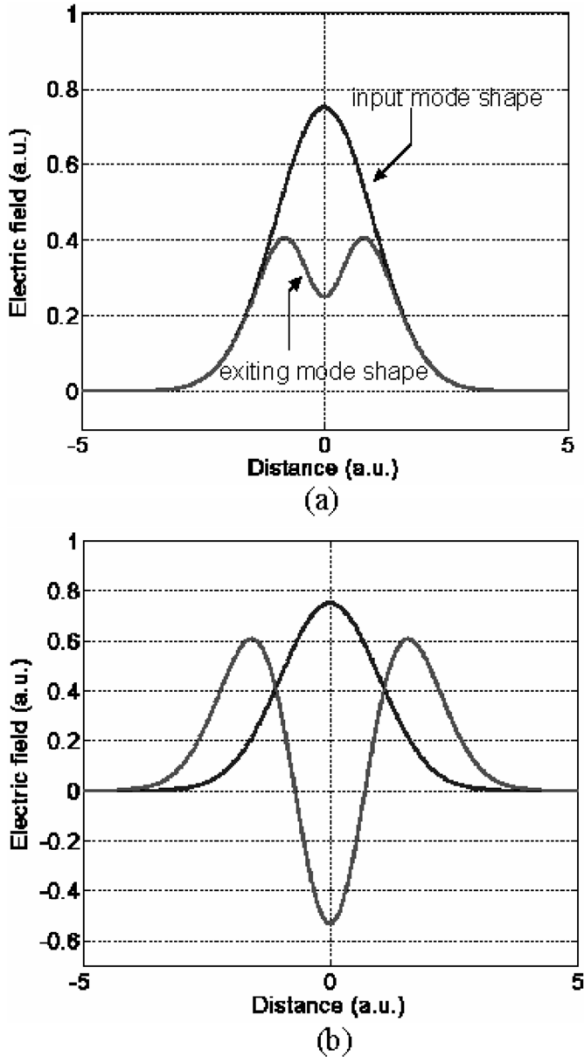


Fig. 9. (a) Illustration of the transverse mode beam shape at the input and output ends of the EAM waveguide. (b) Decomposition of the existing mode shape into first and third order transverse modes.

The single mode fiber at the output provides spatial mode filtering, reducing the transmission in the off state. Fig. 9(a) conceptually illustrates the change in mode shape from propagation in a ridge waveguide with a lossy core material, such as MQW. In the off state, the center of the propagating beam loses intensity due to the location of the QWs. The overlap integral of the exiting beam shape with the fundamental mode of the fiber shown in Fig. 9(b) reveals that only 33% of the exiting power in the off state can be coupled into the exit fiber. This is potentially advantageous since it allows for lower voltage swing operation of the EAM in order to achieve the desired degree of optical transmission modulation.

### A. Switching Bandwidth Characterization

Fig. 10 illustrates the optical setup used for testing. We investigated the optical switching bandwidth of IPS's by measuring the optical $S_{21}$ parameter using an Agilent lightwave component analyzer (LCA), which measures the optical-to-optical transfer function. It has a 1550-nm control beam output which is swept between 130 MHz and 20 GHz. The magnitude of the EAM output power divided by the PD input power as a function of frequency provides a full characterization of the switching behavior of the device, including determination of the 3-dB optical switching bandwidth. As an approximate rule, devices are generally designed with a 3-dB switching bandwidth equal to the desired bit rate for return-to-zero (RZ) operation or half the desired bit rate for nonreturn-to-zero (NRZ) operation. Fig. 11 shows the optical switching bandwidth data together with theoretical simulation results. The simulation parameters are given in Table III.

In the setup, Cascade Microtech Eye Pass electrical probes are used to dc-bias the PD and EAM. The probes incorporate a pair of large parallel bypass capacitors that are located very close to the probe tip ends. The two outer fingers carry the respective PD and EAM biases, while the middle, common finger, is set to ground. The 450-pF bypass capacitors provide isolation between the external circuitry and the devices in the circuit. The probe provides low impedance, resonance-free operation for frequencies up to 20 GHz.

The three different devices in Fig. 11 exhibit 3-dB optical bandwidths of 690 MHz, 1.06, and 2.15 GHz. These measurements were taken with an average PD current of 0.2–1 mA, a PD voltage supply bias of 17 V, an average EAM current of 0.5 mA, and EAM voltage biases of 3–8 V. This set of measurements can be considered a small signal measurement since the optically-induced changes in EAM voltage are on the order of a few tenths of volts. The three sets of Hspice simulations overlaid on this plot exhibit excellent agreement with the experimental data. In Fig. 11, we assumed $|V_{EAM}(\omega)/I_{PD}(\omega)|$, calculated using Hspice, is equal to $|P_{EAM,out}(\omega)/P_{PD,in}(\omega)|$ as measured by the LCA. In this case, a linear change in the EAM voltage translates to a linear change in EAM transmission.

The good agreement between the experimental data and the Hspice simulations validates our circuit model and provides a strong foundation for understanding the overall behavior and scalability of IPS's. The same circuit model is used in simulations for the feasibility study of 10 Gb/s operation in Section III.

### B. Dynamic Behavior Characterization

We demonstrate dynamic operation of IPS's by recording eye diagrams under various conditions using an Agilent Digital Component Analyzer. The eye diagram characteristics depend on the EAM bias, PD bias, EAM input wavelength, and input optical power levels. When the EAM supply voltage is less than 4 V, the EAM is pushed into forward bias during switching and strong electroabsorption characteristics cannot be achieved. In the measurements, the EAM pre-bias was chosen between 4.9 and 10.4 V for optimal performance at each output wavelength. The PD bias was, however, fixed at 17 V. Fig. 12 shows unconstrained, bidirectional wavelength conversion, where eight input and eight output wavelengths were arbitrarily chosen within the C-band (1530.0–1565.0 nm). In all cases, we observed $>$10 dB extinction ratio with $<$8 mW absorbed optical power at 1.25 Gb/s.

It is also possible to couple two different wavelengths into the same EAM waveguide to modulate them simultaneously. Fig. 13 shows wavelength broadcasting over two arbitrarily-chosen channels within the C-band that are separated by 5, 10,

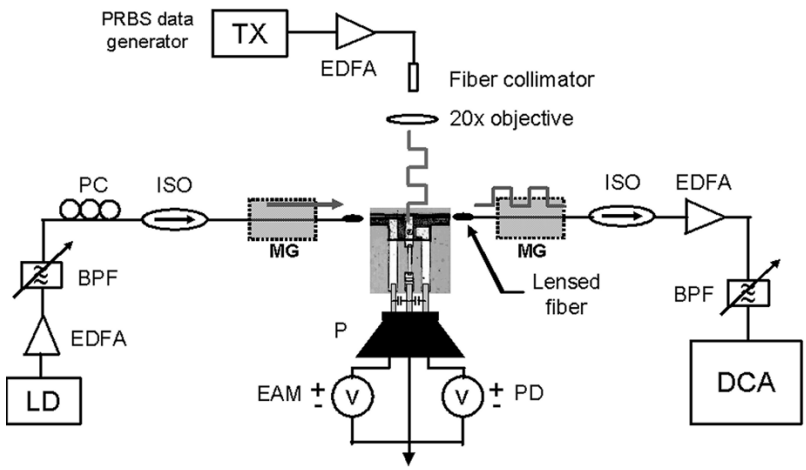


Fig. 10. Illustration of the test setup. Waveguide alignment is done using Melles Griot (MG) six-axis stages. TX: transmitter. EDFA: Erbium-doped fiber amplifier. BPF: band-pass filter. PC: polarization controller. ISO: islator. P: probe. LD: CW-beam laser diode. An Agilent digital component analyzer (DCA) is used with the data generator and the TX for eye diagram measurements. These are replaced with an LCA to measure the optical-to-optical transfer function.

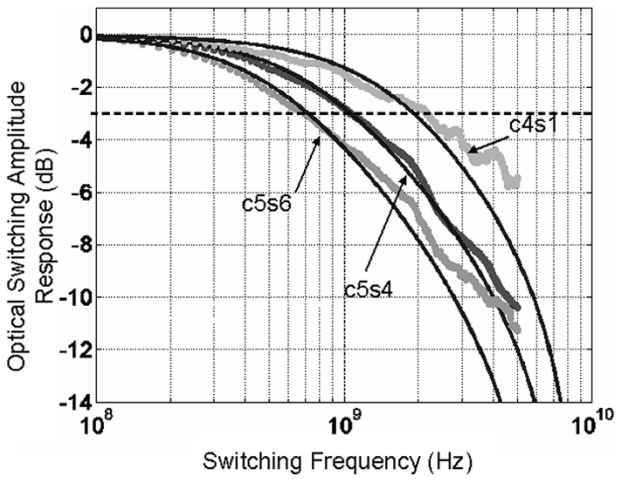


Fig. 11. Optical $S_{21}$ switching bandwidth data overlaid with theoretical simulation results. The simulation parameters are given in Table III.

TABLE III
SIMULATION PARAMETERS USED TO CHARACTERIZE THE OPTICAL $S_{21}$ SWITCHING BANDWIDTH

| Device chip # | c5s6 | c5s4 | c4s1 |
|---|---|---|---|
| $R_{TaN}(\Omega)$ | 650 | 650 | 340 |
| $R_{series,PD}(\Omega)$ | 39 | 38 | 26 |
| $C_{PD}$(fF) | 76 | 76 | 76 |
| $C_{PD\text{-}BCB}$(fF) | 15.6 | 15.6 | 15.6 |
| $R_{series,EAM}(\Omega)$ | 75 | 82 | 120 |
| $w_{EAM}(\mu m)$ | 4.64 | 3.59 | 2.10 |
| $C_{EAM}$(fF) | 338 | 261 | 153 |
| $C_{EAM\text{-}BCB}$(fF) | 16.3 | 19.5 | 24.0 |
| $f_{sim}$(GHz) | 0.74 | 0.97 | 1.95 |
| $f_{exp}$(GHz) | 0.69 | 1.06 | 2.15 |

$C_{PD\text{-}BCB}$ and the $C_{EAM\text{-}BCB}$ are the PD and the EAM parasitic capacitances that exist from the overlap of the *p*-metallization with the conductive *n*-region of these devices. The series resistances are extracted from the IV curves of the individual devices.

or 20 nm. In this measurement, rather than optimizing the EAM bias for a specific wavelength, we applied a high enough bias (e.g., 10 V) to broaden the electroabsorption effect over a sufficiently large wavelength range (e.g., 5, 10, or 20 nm).

Fig. 14(a) illustrates optical switching in NRZ and RZ formats, each with $>$10 dB extinction ratio at 2.5 Gb/s. In Fig. 14(b), we demonstrate 45 nm wavelength conversion range between the output wavelengths of 1525 and 1570 nm at 1.25 Gb/s. This range is limited by the spectral modulation range of the MQW structure as well as the Erbium-doped fiber amplifier placed before the receiver.

### C. Remote Electrical Reconfiguration

We demonstrate two-dimensional (2-D), compact arrays of these switches that monolithically integrate 2-D stacks of surface-normal photodiodes with QW waveguide modulator stacks on a single chip [8]. Such wavelength-converting crossbars provide complete flexibility to selectively convert any of the input wavelengths to any of the output wavelengths at high data bit rates in telecommunication, with the input and output wavelengths being arbitrarily chosen within the C-band. Fig. 15 shows the experimental results.

For these crossbar switches to be useful, it is essential to electrically reconfigure the crossbar switch quickly, such that, by enabling certain switch elements in the array and disabling the rest, the input wavelength channels can be transferred to a desired set of output wavelengths quickly. Individual switch elements perform wavelength conversion provided that their photodiodes and modulators are properly reverse-biased. When slightly forward biased, the photodiodes will not extract photocurrent and the modulators will be transparent. Therefore, each of these switches located at the cross nodes can be rapidly enabled and disabled to reconfigure the crossbar as desired by quickly changing their biases accordingly.

## VI. CONCLUSION

In this paper, we introduce a novel, chip-scale, photonic switching architecture that offers a remedy to the difficulties

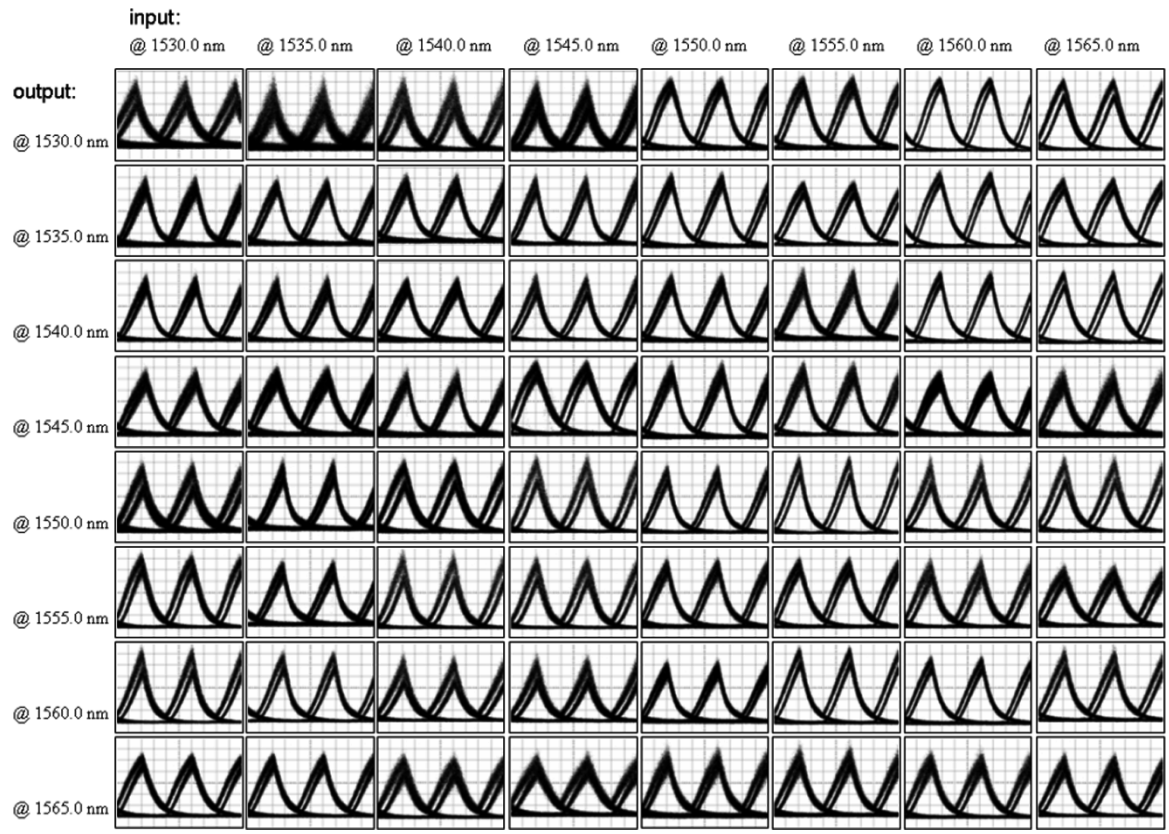


Fig. 12. $8 \times 8$ C-band wavelength conversion matrix for every possible combination of eight input and eight output wavelengths at 1530.0, 1535.0, 1540.0, 1545.0, 1550.0, 1555.0, 1560.0, and 1565.0 nm.

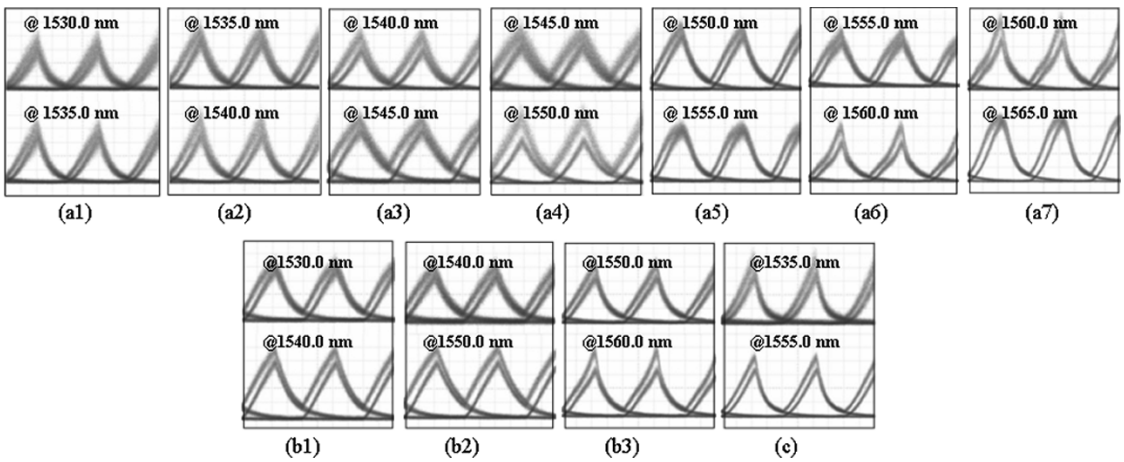


Fig. 13. C-band dual-wavelength broadcasting with channel spacings of 5 nm in (a1)–(a7), 10 nm in (b1)–(b3), and 20 nm in (c).

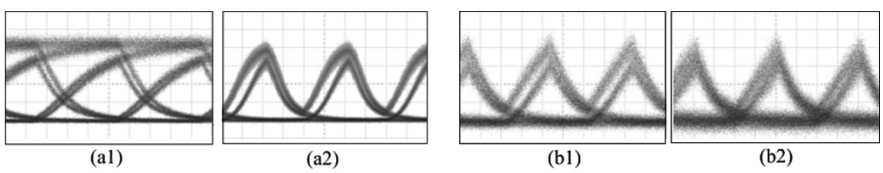


Fig. 14. (a) Optical switching in (1) NRZ and (2) RZ formats with $>10$ dB extinction ratios at 2.5 Gb/s; (b) 45-nm wavelength-conversion range between (b1) 1525.0 and (b2) 1570.0 nm at 1.25 Gb/s.

associated with ordinary o-e-o technology, including fabrication and packaging costs and necessity for large installation space. This photonic switching platform incorporates a MQW waveguide modulator monolithically integrated with a surface-illuminated photodiode. The dual-diode switches exhibit $>10$ dB extinction ratios for gigahertz range switching using only milliwatt-level absorbed optical power across a wide wavelength band. We demonstrate arbitrary wavelength conversion across 45 nm and multiwavelength broadcasting over 20 nm, spanning the entire C-band.

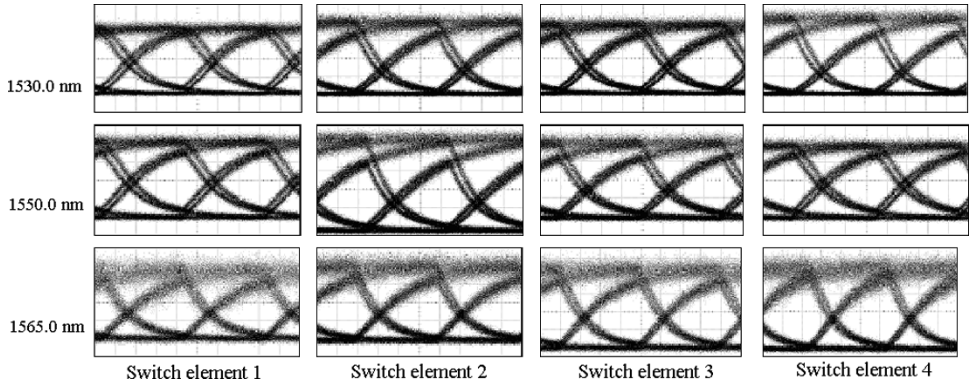


Fig. 15. Eye diagrams from four switch elements in a $2 \times 2$ array for NRZ operation. Output wavelengths are at 1530.0, 1550.0, and 1565.0 nm. All measurements are taken at 1.25 Gb/s, with the input wavelength at 1551.7 nm. (horizontal: 200 ps/div, vertical: $\sim 333\ \mu$W/div).

According to our model, by moderately scaling down the values of the device capacitances and the on-chip thin film resistance, while minimizing parasitics, switch operation at 10 Gb/s should be achievable. By optimizing the electroabsorption properties of the QWs, improving the high-power handling capability of the photodetector, and employing better fabrication techniques that minimize parasitic resistances and capacitances, operation speeds of 40 Gb/s might be achieved. The integration technology we developed can also be extended to include other circuit elements in the structure for additional functionality.

## ACKNOWLEDGMENT

The authors would like to acknowledge OEPIC Corporation for epitaxial wafer growth, and Melles Griot for the waveguide alignment setup.

## REFERENCES

[1] K. G. Koffman and A. M. Odlzko, "Growth of the Internet," AT&T Labs Research, 2001.

[2] ——, *Optical Fiber Communications IV B: Systems and Impairments*, I. P. Kaminov and T. Li, Eds. San Diego, CA: Academic, 2002, pp. 17–56.

[3] . [Online]http://www.jpix.ad.jp/en/techncal/traffic.html

[4] K. Shimano, T. Takahashi, M. Koga, and Y. Takigawa, "Technical improvements in photonic networks for constructing next generation networks," *NTT Tech. Rev.*, vol. 1, no. 8, pp. 12–23, 2003.

[5] V. A. Sabnis, H. V. Demir, O. Fidaner, J. S. Harris Jr., D. A. B. Miller, J.-F. Zheng, N. Li, T.-C. Wu, H.-T. Chen, and Y.-M. Houng, "Optically-controlled electroabsorption modulators for unconstrained wavelength conversion," *Appl. Phys. Lett.*, vol. 84, no. 4, pp. 469–471, 2004.

[6] H. V. Demir, V. A. Sabnis, O. Fidaner, J. S. Harris Jr., D. A. B. Miller, and J.-F. Zheng, "Dual-diode quantum-well modulator for C-band wavelength conversion and broadcasting," *OSA Opt. Exp.*, vol. 12, no. 2, pp. 310–316, 2004.

[7] H. V. Demir, V. A. Sabnis, J.-F. Zheng, O. Fidaner, J. S. Harris Jr., and D. A. B. Miller, "Scalable wavelength-converting crossbar switches," *IEEE Photon. Technol. Lett.*, vol. 16, no. 10, pp. 2305–2307, Oct. 2004.

[8] S. J. B. Yoo, "Wavelength conversion technologies for WDM network applications," *J. Lightw. Technol.*, vol. 14, no. 6, pp. 955–966, June 1996.

[9] J. Hutchinson, J.-F. Zheng, J. S. Barton, M. L. Masanovic, M. N. Sysak, J. A. Henness, L. A. Johansson, D. J. Blumenthal, L. A. Coldren, H. V. Demir, V. A. Sabnis, O. Fidaner, J. S. Harris Jr., and D. A. B. Miller, "Indium phosphide based wavelength conversion for high speed optical networks," *Intel Technol. J.*, vol. 8, no. 2, pp. 161–171, 2004.

[10] L. A. Coldren, "Widely-tunable chip-scale transmitters and wavelength converters," in *Proc. OSA Conf. Integrated Photonics Research (IPR), OSA Tech. Dig.*. Washington, DC, 2003, pp. 6–8.

[11] S. Kodama, T. Ito, N. Watanabe, S. Kondo, H. Takeuchi, H. Ito, and T. Ishibashi, "200 Gb/s monolithic photodiode-electroabsorption modulator optical gate," in *Proc. Device Research Conf.*, Notre Dame, IN, 2001, pp. 151–152.

[12] H. Yasaka, M. Okuno, and H. Sugahara, "Device technologies for photonic networks," *NTT Tech. Rev.*, vol. 1, no. 8, pp. 49–59, 2003.

[13] J.-L. Oudar, "Ultrafast semiconductor all-optical processing devices for telecommunication applications," in *Proc. Ultrafast Photonics Workshop*, 2004.

[14] S. Hardy, "Infinera touts the benefits of OEO," *Lightwave*, May 3, 2004.

[15] C. Matsumoto, "Infinera declares WDM war," *Lightreading*, May 3, 2004.

[16] D. A. B. Miller, "Ultrafast quantum well optoelectronic devices," U.S. Patent 6 445 839, Sep. 3, 2002.

[17] H. V. Demir, D. A. B. Miller, and V. A. Sabnis, "Semiconductor device for rapid optical switching by modulated absorption," US Patent 6 680 791, Jan. 20, 2004.

[18] M. B. Yairi, C. W. Coldren, D. A. B. Miller, and J. S. Harris Jr., "High speed, optically controlled surface-normal optical switch based on diffusive conduction," *Appl. Phys. Lett.*, vol. 75, no. 5, pp. 597–599, 1999.

[19] M. B. Yairi, H. V. Demir, and D. A. B. Miller, "Optically controlled optical gate with an optoelectronic dual diode structure: theory and experiment," *J. Opt. Quantum Electron.*, vol. 33, no. 7–10, pp. 1035–1054, 2001.

[20] V. A. Sabnis, H. V. Demir, M. B. Yairi, J. S. Harris Jr., and D. A. B. Miller, "High-speed, optical switching based on diffusive conduction in an optical waveguide with surface-normal optical control," *J. Appl. Phys.*, vol. 95, no. 5, pp. 2258–2263, 2004.

[21] K. Kato, "Ultra wideband/high-frequency photodetectors," *IEEE Trans. Microwave Theory Tech.*, vol. 47, no. 7, pp. 1265–1281, Jul. 1999.

[22] D. A. B. Miller, D. S. Chemla, T. C. Damen, A. C. Gossard, W. Wiegmann, T. H. Wood, and C. A. Burrus, "Bandedge electro-absorption in quantum well structures: The quantum confined stark effect," *Phys. Rev. Lett.*, vol. 53, pp. 2173–2177, 1984.

[23] S. Zhang, "Traveling-wave electroabsorption modulators," Ph.D. dissertation, Univ. California, Santa Barbara, CA, 1999.

[24] V. A. Sabnis, H. V. Demir, O. Fidaner, J. S. Harris Jr., D. A. B. Miller, J.-F. Zheng, N. Li, T.-C. Wu, and Y.-M. Houng, "Optically-switched dual-diode electroabsorption modulators," in *Proc. OSA Conf. Integrated Photonics Research (IPR), OSA Tech. Dig*. Washington, DC, 2003, Pap. IMB3, pp. 12–14.

[25] J.-F. Zheng, J. P. Hanberg, H. V. Demir, V. A. Sabnis, O. Fidaner, J. S. Harris Jr., and D. A. B. Miller, "Novel passivation and planarization in the integration of III-V semiconductor devices," in *Proc. SPIE Photonics West Conf.*, San Jose, CA, Jan. 24–29, 2004, Pap. 5356-9.

[26] H. V. Demir, J.-F. Zheng, V. A. Sabnis, O. Fidaner, J. P. Hanberg, J. S. Harris Jr., and D. A. B. Miller, "Self-aligning planarization and passivation in the integration of III-V semiconductor devices," *IEEE Trans. Semicond. Manuf.*, vol. 8, no. 1, pp. 1–8, Feb. 2005.

**Hilmi Volkan Demir** (S'98) received the B.Sc. degree in electrical and electronics engineering from Bilkent University, Ankara, Turkey, in 1998, and the M.S. and Ph.D. degrees in electrical engineering from Stanford University, CA, in 2000 and 2004, respectively. His doctoral research focused on invention, design, fabrication, testing, and modeling of multifunctional integrated photonic switches. His Ph.D. dissertation led to the world's first wavelength-converting crossbar switches.

In September 2004, he joined Bilkent University, where he is currently an Assistant Professor of physics. He is also Associate Director of Bilkent Nanotechnology Research Center and a Faculty Member of Bilkent Advanced Research Laboratory. He has published over 20 journal and conference papers, presented over ten invited talks, cotranslated two books, and disclosed four U.S. patents (two filed, one allowed, one continuation).

Dr. Demir is a recipient of the Stanford Intel Research Assistantship (2000–2004), the Edward L. Ginzton Fellowship (1998–1999), and the Bilkent Board of Trustees Scholarship (1994–1998). He was one of the Stanford-Berkeley Innovator's Challenge Finalists, CA, in 2003 and an invited participant of London International Youth Science Forum, U.K., in 1994.

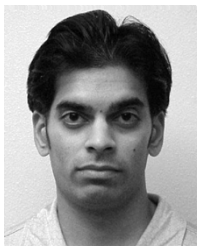

**Vijit A. Sabnis** (S'96) received the B.Sc. degree (highest honors, honors program) in electrical engineering and computer sciences from the University of California, Berkeley, in 1995, and the M.S. and Ph.D. degrees in electrical engineering from Stanford University, Stanford, CA, in 1997 and 2003, respectively. His doctoral research was conducted in the areas of epitaxial growth, fabrication, simulation, and characterization of optically controlled electroabsorption modulators.

**Onur Fidaner** (S'00) received the B.Sc. degree in electrical and electronics engineering from Middle East Technical University, Ankara, Turkey, in 2001, and the M.S. degree in electrical engineering from Stanford University, Stanford, CA, in 2003. He is currently a Lucent Technologies Stanford Graduate Fellowship Student at Stanford University, where he is working towards the Ph.D. degree in electrical engineering.

His research interests include the development of novel integrated photonic devices incorporating quantum-well structures for future optical networks.

**Jun-Fei Zheng** received the Ph.D. degree in materials science from University of California, Berkeley, in 1994.

Since 1994, he has been with Intel Corporation, Santa Clara, CA, where he is working on Silicon process technology development, advanced MOS transistors, and photonic and optoelectronic devices. He was with Intel Strategic Technology Group and was an Intel researcher-in-residence at Stanford University, Stanford, CA, from 2001 to 2004. Currently, he is a Senior Staff Scientist with th eIntel Strategic Technology Group and also an Intel Visiting Fellow at Yale University, New Haven, CT.

**James S. Harris, Jr.** (S'65–M'69–SM'78–F'88) received the B.S., M.S., and Ph.D. degrees in electrical engineering from Stanford University, Stanford, CA, in 1964, 1965, and 1969, respectively.

In 1969, he joined the Rockwell International Science Center, Thousand Oaks, CA, where he was one of the key contributors in developing their preeminent position in GaAs device technology. In 1982, he joined the Solid State Electronics Laboratory, Stanford University, as Professor of Electrical Engineering. He served as Director of the Solid State Electronics Laboratory (1984–1998) and the Joint Services Electronics Program (1985–1999), Stanford University. He is currently the James and Ellenor Chesebrough Professor of Engineering at Stanford University. He has supervised over 65 Ph.D. students, has over 650 publications, and 14 issued U.S. patents. His current research interests are in the physics and application of ultrasmall structures and novel materials to new high-speed and spin-based electronic and optoelectronic devices and systems.

Dr. Harris is a Fellow of the American Physical Society. He received the 2000 IEEE Morris N. Liebmann Memorial Award, the 2000 International Compound Semiconductor Conference Walker Medal, an IEEE Third Millennium Medal, and an Alexander von Humboldt Senior Research Prize in 1998 for his contributions to GaAs devices and technology.

**David A. B. Miller** (M'84–SM'89–F'95) received the B.Sc. degree from St. Andrews University, Fife, Scotland, U.K., and the Ph.D. degree from Heriot-Watt University, Edinburgh, Scotland, in 1979.

He was with Bell Laboratories, Holmdel, NJ, from 1981 to 1996, as a Department Head from 1987, latterly of the Advanced Photonics Research Department. He is currently the W. M. Keck Professor of Electrical Engineering at Stanford University, Stanford, CA, and the Director of the Ginzton and Solid State and Photonics Laboratories, Stanford, CA. He has published more than 200 scientific papers, and holds over 55 patents. His research interests include quantum-well optoelectronic and nanophotonic physics and devices, and fundamental and applications of optics in information, sensing, switching, and processing.

Dr. Miller has served as a Board Member for both the Optical Society of America (OSA) and IEEE Lasers and Electro-Optics Society (LEOS), and in various other society and conference committees. He was President of the IEEE Lasers and Electro-Optics Society in 1995. He was awarded the Adolph Lomb Medal and the R. W. Wood Prize from the OSA, the International Prize in Optics from the International Commission for Optics, and the IEEE Third Millennium Medal. He is a Fellow of the Royal Societies of London and Edinburgh, OSA, and the American Physical Society, and holds honorary degree from the Vrije Universiteit Brussel and Heriot-Watt University.